nature nanotechnology

LETTERS

https://doi.org/10.1038/s41565-020-00804-0

Check for updates

Optical control of the valley Zeeman effect through many-exciton interactions

Weijie Li[1,2], Xin Lu[1,2], Jiatian Wu[1,2] and Ajit Srivastava[1]✉

Charge carriers in two-dimensional transition metal dichalcogenides (TMDs), such as WSe_2, have their spin and valley-pseudospin locked into an optically addressable index that is proposed as a basis for future information processing[1,2]. The manipulation of this spin–valley index, which carries a magnetic moment[3], requires tuning its energy. This is typically achieved through an external magnetic field (*B*), which is practically cumbersome. However, the valley-contrasting optical Stark effect achieves valley control without *B*, but requires large incident powers[4,5]. Thus, other efficient routes to control the spin–valley index are desirable. Here we show that many-body interactions among interlayer excitons (IXs) in a $WSe_2/MoSe_2$ heterobilayer (HBL) induce a steady-state valley Zeeman splitting that corresponds to $B \approx 6$ T. This anomalous splitting, present at incident powers as low as microwatts, increases with power and is able to enhance, suppress or even flip the sign of a *B*-induced splitting. Moreover, the *g*-factor of valley Zeeman splitting can be tuned by ~30% with incident power. In addition to valleytronics, our results could prove helpful to achieve optical non-reciprocity using two-dimensional materials.

The magnetic control of valley pseudospin, through the valley Zeeman effect, is well-established in monolayer[6–9] and HBL TMDs[10–13]. Whereas the above-mentioned approaches for valley control are based on single-exciton effects, a magnetic field can also arise through many-particle interactions when there is an imbalance in the densities of the two spin species. Although a valley splitting by a magnetic proximity effect has been observed[14–16], it is natural to ask whether an optically tunable valley control based on many-exciton interactions can be realized in TMDs to expand the toolkit of valleytronics. To this end, we investigated IXs in the HBL of $WSe_2/MoSe_2$. The type-II band alignment of this HBL results in IXs with electrons (holes) confined in the Mo (W) layer that have a permanent electric dipole with a fixed orientation in the out-of-plane direction[12,17,18]. The exciton–exciton interaction among IXs can be approximated by two terms—a valley-independent dipolar repulsion term, U_{dd}, and a valley-dependent exchange interaction term, U_{ex}, which raises or lowers, respectively, the energy of a parallel or an antiparallel, respectively, alignment of spin–valley indices[17–19]. In a simple picture, we can understand the higher energy of the ferromagnetic alignment in the presence of repulsive interactions due to the bosonic nature of the excitons, unlike the nature of electrons.

Figure 1a demonstrates the basic idea behind our scheme. In a many-exciton scenario, U_{dd} results in a exciton density-dependent blueshift[20], whereas U_{ex} results in an exchange-induced mean field (B_{ex}), which depends on the imbalance, $\Delta n = n_+ - n_-$, in the exciton densities ($n_\pm$) at the two spins or valleys[19,21–23]. When populations of $\pm K$ excitons are the same, time-reversal symmetry is unbroken and the two valleys remain degenerate. For a finite Δn, any given exciton experiences B_{ex} whose direction depends on the sign of Δn such that its energy is raised (lowered) if it belongs to the valley with the majority (minority) of excitons. In particular, the optically recombining excitons also experience B_{ex} and the resulting valley splitting can be measured in a helicity-resolved emission spectra.

Figure 1b shows an optical microscope image of our fabricated heterostructure with monolayer $MoSe_2$ on top of WSe_2 with aligned edges (0 or 60°). Its photoluminescence (PL) spectrum at 4 K exhibits a peak at ~1.40 eV (Fig. 1c), which is in the typical IX energy range[10,11]. The strong emission intensity with an integrated (peak) intensity that exceeds $3{,}400 \times 10^3$ counts per second (c.p.s.) (25×10^3 c.p.s.) at a low excitation power of 1 μW, demonstrates a high efficiency to create IXs at low powers (Methods). To further confirm the interlayer nature of the peak, we conducted photoluminescence excitation (PLE) spectroscopy. The PLE spectrum in Fig. 1d shows two prominent resonances at 1.64 and 1.72 eV, which correspond to the monolayer $MoSe_2$ and WSe_2 intralayer exciton states, respectively, as is expected for IX.

To optically create Δn, we exploited the valley-contrasting optical selection rules for circular absorption in TMDs[2,19]. By circularly polarized excitation, say at the WSe_2 exciton resonance, Δn can be efficiently created first in the WSe_2 layer, which should then get transferred to the long-lived (nanoseconds) IX on a very short timescale (< 50 fs) (refs. [24,25]). The spin–valley locking and the strong suppression of contact-type electron–hole exchange interaction in IXs is expected to reduce any valley mixing during the relaxation of an intralayer exciton to IX. This, together with the long IX lifetime[19,26], should lead to an efficient generation of Δn in the steady state, even at low excitation powers.

We first confirmed the generation of Δn between the $|\mathrm{IX}, +\rangle$ and $|\mathrm{IX}, -\rangle$ exciton densities, where $|\mathrm{IX}, \pm\rangle$ denote the IXs in the $\pm K$ valleys. The imbalance can be characterized by the valley polarization or the degree of circular polarization (DCP) of PL, which is defined as $(I_{co} - I_{cross})/(I_{co} + I_{cross})$, where I_{co} (I_{cross}) is the intensity of the co-polarized (cross-polarized) emission peak under circularly polarized excitation. Fig. 2a shows that only excitation close to the WSe_2 resonance (1.72 eV) can create a large positive DCP, whereas $MoSe_2$ resonance (1.64 eV) produces negligible DCP (see Supplementary section 1). This large positive DCP for WSe_2 resonance indicates that IX is co-polarized with the excitation helicity that is, co-polarized excitons have much higher density leading to a large imbalance between two valleys.

Next, we controlled Δn by varying the intensity of the circular excitation resonant with the WSe_2 exciton and performed helicity-resolved PL spectroscopy at a low power (0.3 μW; Fig. 2b) and high power (10 μW; Fig. 2c). With σ^+ (σ^-) excitation, the σ^+ (σ^-) emission is more intense, which highlights the co-polarized

[1]Department of Physics, Emory University, Atlanta, GA, USA. [2]These authors contributed equally to this work: Weijie Li, Xin Lu, Jiatian Wu.
✉e-mail: ajit.srivastava@emory.edu

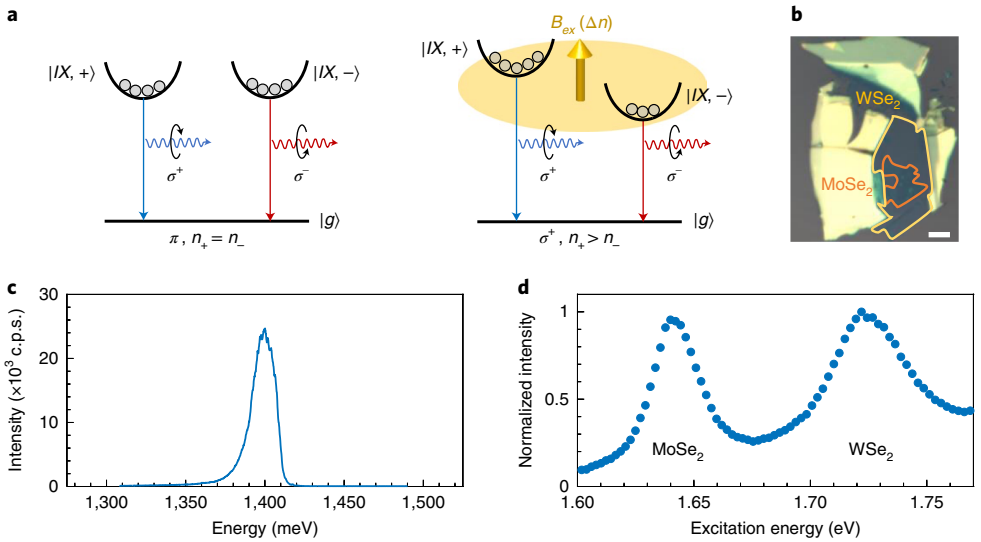

Fig. 1 | Many-exciton exchange interactions among IXs with a $WSe_2/MoSe_2$ heterostructure. a, Schematic of IX valley energies under linear (π) and circular (σ) excitation. The valley IXs emit σ^+ (σ^-) light in the state $|\mathrm{IX}, +\rangle$ ($|\mathrm{IX}, -\rangle$) and $|g\rangle$ is the exciton ground state. The populations of excitons, $n_\pm$, in the ±K valleys under π excitation (left panel) are the same, whereas σ^+ excitation (right panel) induces an imbalance, $\Delta n = n_+ - n_- > 0$. The imbalance under σ^+ excitation makes the exchange interaction between $|\mathrm{IX}, +\rangle$ excitons larger when compared with π excitation and gives rise to an effective exchange field $B_{ex}(\Delta n)$, shown by the yellow shaded region and arrow. **b**, Optical microscope image of a $WSe_2/MoSe_2$ HBL sample. The WSe_2 ($MoSe_2$) flakes are outlined in yellow (orange). Scale bar, 5 μm. **c**, The PL spectrum of the IX at 4 K shows a strong peak at ~1,400 meV under 1 μW excitation power. **d**, PLE intensity plot showing two prominent resonances at 1.64 and 1.72 eV, which correspond to the monolayer $MoSe_2$ and WSe_2 intralayer exciton states. The intensity is integrated over the PL peak in **c**. The excitation energy is 1.72 eV in **c** and the excitation power is 2 μW in **d**.

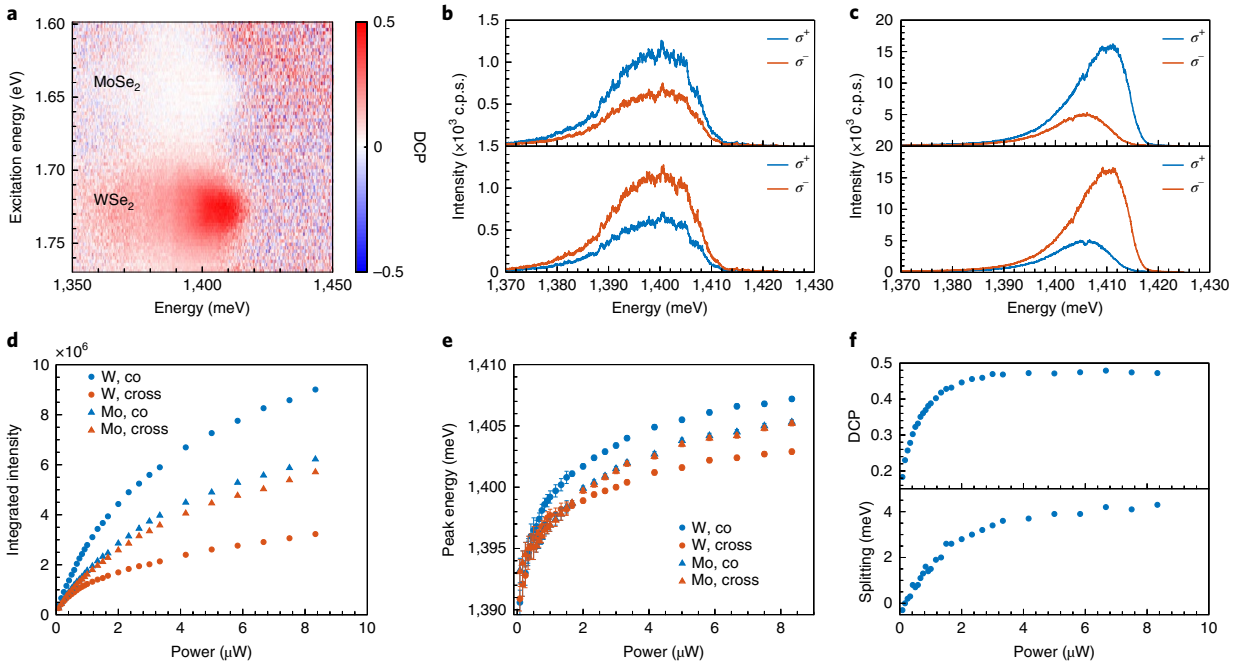

Fig. 2 | Exchange field-induced splitting in $WSe_2/MoSe_2$ heterostructure. a, The excitation energy dependence of the DCP defined as $(I_{co} - I_{cross})/(I_{co} + I_{cross})$. I_{co} (I_{cross}) is the intensity of the co-polarized (cross-polarized) IX. An excitation at the WSe_2 ($MoSe_2$) resonance of ~1.72 eV (1.64 eV) creates a large (negligible) DCP, which implies a large (negligible) imbalance between two valley IX populations. **b**,**c**, Helicity-resolved PL spectra of interlayer excitons under low (high) excitation power of 0.3 μW (10 μW) shown in **b** (**c**). The sample is excited with σ^+ (σ^-) light in the top (bottom) panels at 1.72 eV. At a low power (**b**), no apparent splitting between the σ^+ and σ^- components is observed, whereas an obvious splitting is observed at a high power (**c**). The co-polarized (co) peaks have a higher intensity than that of the cross-polarized (cross) peaks. **d**,**e**, Power dependence of the integrated intensities and peak energies at the WSe_2 ($MoSe_2$) resonance denoted by circles (triangles). The co-polarized (cross-polarized) peak is shown in blue (red). At the WSe_2 resonance, the imbalance between intensities of co- and cross-polarized peaks and their peak energies increases with power, unlike for the $MoSe_2$ resonance. The error bar in **e** results from the uncertainty in the fitting of the peak position. **f**, Power dependence of DCP and splitting at the WSe_2 resonance. The splitting energy is $E_{co} - E_{cross}$, where E_{co} (E_{cross}) is the energy of the co-polarized (cross-polarized) peak and follows the same trend as that of DCP, that is, increases with power and then saturates at high powers. The excitation power is 2 μW in **a**. **a**,**d**–**f** and **b**,**c** are two sets of data collected in different set-ups and different thermal cycles.

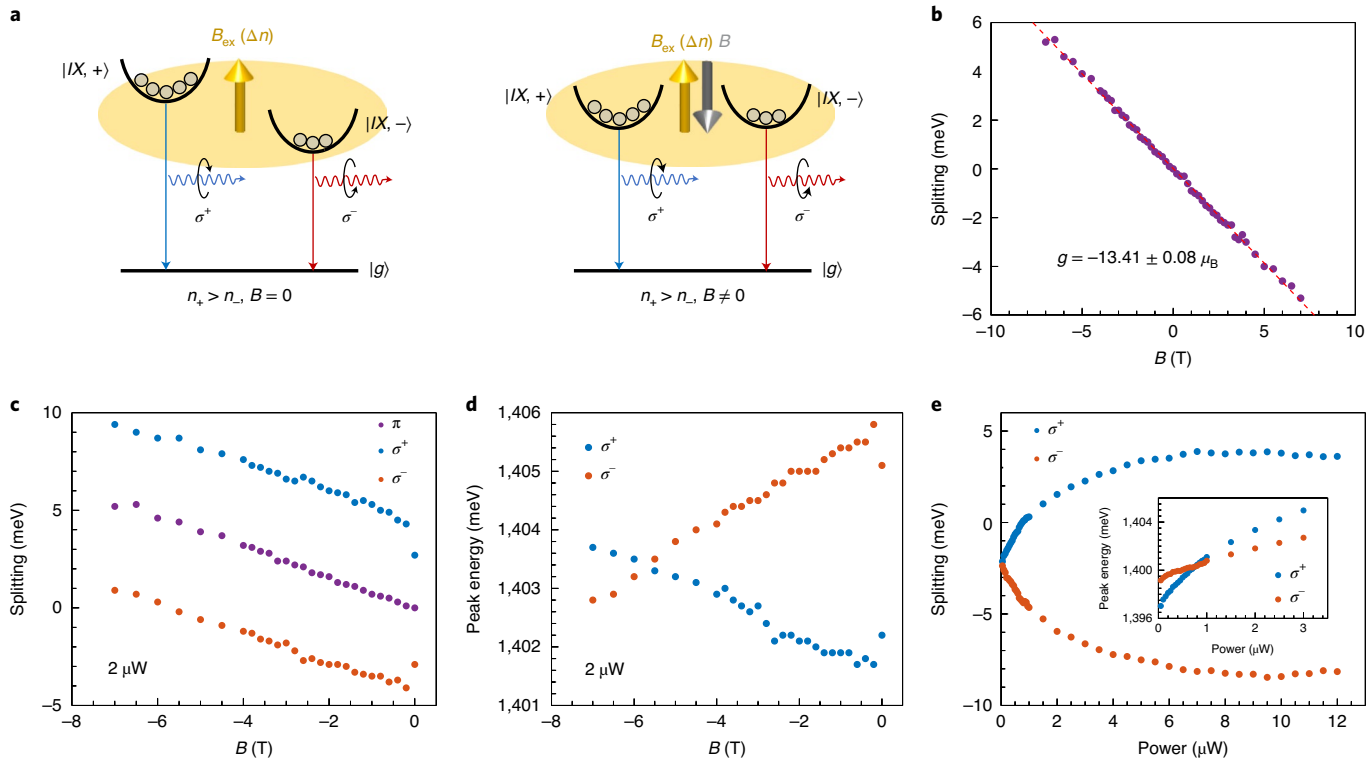

Fig. 3 | Equivalence between the exchange field and the external magnetic field. a, Schematic of valley IX energy levels at $B=0$ and $B\neq0$ under σ^+ excitation. At $B=0$ (left panel), the circular excitation creates an exchange field B_{ex} (yellow arrow) that lifts the degeneracy of the two valley IXs. By applying an external B (right panel, grey arrow), B_{ex} can be cancelled. **b**, B dependence of the Zeeman splitting energy ($E_{\sigma^+}-E_{\sigma^-}$) under linear excitation. The g-factor of -13.41 is consistent with a 60° stacking angle. The pink dashed line is the linear fitting of the data. The error is from the uncertainty of linear fitting of the splitting. μ_B, Bohr magneton. **c**, B dependence of the splitting energy under circular excitation. At an excitation power of 2 μW, the splitting energy of the circular excitation ($E_{\sigma^+}-E_{\sigma^-}$) is equal to the B_{ex}-induced splitting plus the Zeeman splitting under linear excitation. **d**, B dependence of the peak energies under σ^- excitation. The energies of the σ^+ and σ^- components are flipped by the external B of -6 T. Thus, σ^- excitation is equivalent to a positive B_{ex}. **e**, Power dependence of the splitting energies under circular excitation at $B=3$ T. At low (high) powers, the splitting is roughly equal to (larger than) the Zeeman splitting under linear excitation. Inset: peak energy shift with the excitation power of σ^+ showing a flip of ~0.8 μW, which indicates that the σ^+ excitation is equivalent to a negative B. The excitation energy is 1.72 eV for all the panels.

behaviour. At a low circular power, the co-polarized emission has the same energy as the cross-polarized peak within the spectral resolution, whereas at a higher circular power, where a large Δn is expected, the co-polarized emission for both helicities of the excitation blueshifts compared with the cross-polarized peak. Moreover, the PL spectra under linearly polarized excitation does not result in any splitting and falls between the two circular excitation spectra (Supplementary Section 1). In other words, circular excitation effectively breaks time-reversal symmetry and leads to an anomalous valley splitting at zero external B. The co-polarized emission with a higher intensity has a higher energy, consistent with the effect of B_{ex} shown in Fig. 1a. The zero-field splitting at a modest continuous-wave power of 10 μW is ~4.5 meV, which, based on the IX g-factor discussed below, is equivalent to $B\approx6$ T.

Our observations should be contrasted with a recent report of a zero B valley splitting observed in a similar TMD HBL wherein the lower intensity, cross-polarized peak shifts to a higher energy and the splitting decreases with increasing circular power[27]. In our case the stronger emission peak, that is, higher exciton density, is blueshifted, whereas in Jiang et al.[27], the stronger emission peak is redshifted. This qualitatively different behaviour cannot arise from valley splitting induced by exciton interaction and was attributed to an asymmetry in the valley relaxation times of electrons and holes. However, our findings are similar to the helicity-induced Zeeman splitting of excitons in GaAs quantum wells, under transient conditions, which originate from many-exciton interactions[21,22]. We also remark that a laser intensity as low as 100 W cm^{-2} is required to observe a valley-splitting of 1 meV in our scheme as opposed to ~GW cm^{-2} required to obtain a similar splitting using the valley-contrasting optical Stark effect[4,5]. Owing to the incoherent efficient charge transfer in the IX formation, the coherent effects, such as the optical Stark effect and dressed states, have a negligible contribution to the anomalous splitting (Supplementary Section 8).

We performed a systematic power dependence under circular excitation at both the WSe_2 and $MoSe_2$ resonances. With increasing power, the integrated intensities increased and saturated (Fig. 2d) and the peak energies blueshifted (Fig. 2e). The saturation of the total intensity with power possibly arises from exciton–exciton annihilation. The estimated low exciton–exciton annihilation rate is in agreement with the negligible optical doping, and thus exciton–polaron interaction plays a negligible role in our system (Supplementary Section 2). The blueshift results from both U_{dd} and U_{ex} between IXs.

For the WSe_2 resonance, we converted the difference in the integrated intensities (peak energies) into DCP (splitting), as shown in Fig. 2f (and Supplementary Section 3). The DCP increases from 20 to 50% and saturates beyond 3 μW, with a similar trend for the splitting, which increases from 0 to ~4.5 meV (see Supplementary Section 4 for additional data). Using a model based on exciton–exciton interactions (Supplementary Section 5), the calculated splitting from the peak shifts and DCP reproduced the experimental results fairly well, which supports the fact that the splitting arises

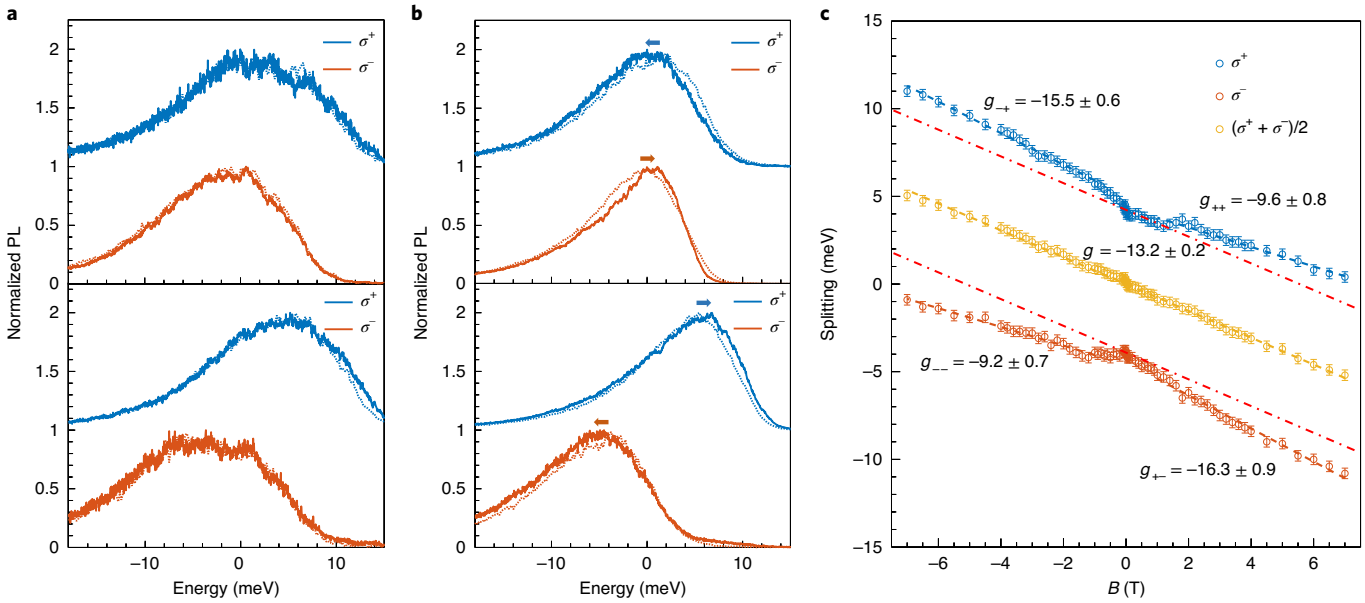

Fig. 4 | Non-linear behaviour of Zeeman splitting under a large circular excitation power. a,**b**, Normalized PL spectra with an excitation power of 1 μW (**a**) and 7.6 μW (**b**) at $B = -7$ T. The top (bottom) panel shows spectra excited by σ^- (σ^+) light. To show the splitting in a symmetric fashion, the zero of the energy is defined as the midpoint of fitted peak positions of the σ^+ and σ^- components. The blue and red dashed lines in **a** and **b** are the expected peaks at −7 T obtained by shifting the 0.1 T peaks by the corresponding Zeeman energy for a linear excitation. At a low circular power (**a**), the experimental data match the expected curve, which implies that the *g*-factor is independent of the excitation polarization. At a high circular power (**b**), σ^+ (σ^-) excitation enhances (cancels) the splitting more than expected, as shown by the left and right pointing arrows, which implies a non-linear behaviour in power and *B*. The σ^+ emission is offset for clarity. **c**, *g*-factors of different excitation polarizations at an excitation power of 7.6 μW. The *g*-factor of the σ^+ (σ^-) excitation under negative (positive) *B* is −15.5 (−16.3), which is larger than the linear case and consistent with **b**. In contrast, σ^- (σ^+) excitation under a negative (positive) *B* has a smaller *g*-factor. The error bars in **c** result from the uncertainty in the fitting of the peak position. The blue and red dashed lines are linear fits for the σ^+ and σ^- excitations, and the yellow line is the average of the two, excluding the dip near 0 T. The red dashed dot lines are parallel to the fitting curve of the averaged data, which has a *g*-factor close to the linear case. The excitation energy is 1.72 eV for all the panels.

from the imbalance between $|\mathrm{IX}, +\rangle$ and $|\mathrm{IX}, -\rangle$. Assuming a binding energy of $E_b = 200$ meV, and a Bohr radius of $a_B = 2$ nm, we estimate that a splitting of ~4 meV arises from $\Delta n \approx 5 \times 10^{11}\,\mathrm{cm}^{-2}$. This estimate agrees well for an incident power in the microwatts range with an absorption of ~10% at the WSe_2 resonance and IX lifetime of nanoseconds (Supplementary Section 5). We extracted the strength of the exciton–exciton interaction from our experiments to be ~0.8 μeV μm^2, which is about an order of magnitude larger than those of previous studies on monolayer TMDs[28–31] and is comparable to those of GaAs quantum well excitons[21,22]. Owing to their longer lifetime, a steady-state Δn was efficiently created in the TMD HBL as opposed to that in GaAs quantum wells.

To further investigate the analogy between B_{ex} and *B*, we performed magnetophotoluminescence spectroscopy. As shown in Fig. 3a, σ^+ pumping induces an imbalance between $|\mathrm{IX}, +\rangle$ and $|\mathrm{IX}, -\rangle$ at $B = 0$, and thus the energy of $|\mathrm{IX}, +\rangle$ is higher than that of $|\mathrm{IX}, -\rangle$. When an external *B* is applied perpendicular to the sample ($B \neq 0$), it shifts the energies of the two valleys in opposite directions, by the valley Zeeman effect, depending on the direction of the out-of-plane *B* (refs. [10–12]). Thus, we expect an external *B* to cancel B_{ex} in one direction and enhance it in the other. We first characterized the Landé *g*-factor of our HBL by measuring the valley Zeeman effect[32–35] under a linearly polarized excitation. As shown in Fig. 3b, we measured a *g*-factor of −13.41, which suggests that the sample is stacked with a twist angle ~60° (ref. [10]). The fact that we observed only one co-polarized peak with a *g*-factor of −13.41 is consistent with an optically bright spin triplet state at a H_n^h stacking, whereas the cross-polarized spin singlet state is a higher energy state and suppressed at low temperatures (Supplementary Section 1)[11].

Figure 3c shows that for σ^+ (σ^-) excitation, the magnitude of splitting increases (decreases) from 0 to −6 T. Thus, the B_{ex} generated by σ^+ (σ^-) excitation acts in concert (opposition) with the negative *B*. We note that the 'dip' in the splitting near 0 T is reminiscent of a similar behaviour in DCP of long-lived excitons in TMDs under tiny *B* (refs. [36,37]) (also see Supplementary section 6). From Fig. 3d, we find that the effect of the anomalous splitting at $B = 0$ is completely cancelled by the external $B \approx -6$ T for σ^- excitation and the energies of $|\mathrm{IX}, +\rangle$ and $|\mathrm{IX}, -\rangle$ are flipped beyond −6 T (Fig. 3d). The ability to optically undo the effect of *B* up to 6 T with continuous-wave power of microwatts is attractive for spin–valley control, which has not been previously observed[21,22,27].

Another evidence for the equivalence between B_{ex} and external *B* is shown in Fig. 3e, where we fix the external *B* at +3 T and vary the circular excitation power. At very low powers, B_{ex} is negligible and the splitting of −2.3 meV is the same as the Zeeman splitting under linear excitation at +3 T in Fig. 3b. When the power increases, the exchange field induced by σ^+ excitation cancels the external *B* at ~0.8 μW. The inset of Fig. 3e clearly shows that a flip in the energies of the two valleys at a positive *B* is caused by σ^+ excitation. Thus, we can conclude that σ^+ (σ^-) excitation results in B_{ex} acting as a negative (positive) external *B*.

From Fig. 3c, it appears that the splitting under $\sigma^\pm$ excitation is merely shifted from the Zeeman splitting under linear excitation by about ±4 meV, such that the *g*-factor is independent of the helicity of excitation. One can ask whether the total splitting, in the presence of circular excitation and *B*, is simply a sum of zero-field splitting and the valley Zeeman splitting for linearly polarized excitation. To answer this question, we first studied the *B* dependence at low circular power of 1 μW. As shown in the Fig. 4a, at −7 T, the expected

spectra (dashed lines), assuming a linear behaviour obtained by shifting the 0.1 T data by the corresponding Zeeman splitting under linear excitation, match very well with the measured spectra (solid lines). Therefore, we can conclude that there is negligible non-linear behaviour in the splitting at low powers. As shown in Fig. 4b, at a higher circular power (7.6 μW), the expected spectra at −7 T and the measured spectra have a small but systematic difference. We find that the σ^- (σ^+) excitation, which should reduce (enhance) the splitting, reduces (enhances) the splitting more than expected, which implies a larger magnitude of B_{ex}. When the external B is flipped, a similar behaviour is seen with the roles of $\sigma^{\pm}$ interchanged.

To understand this non-linear behaviour further, we performed a systematic B dependence analysis and found that it led to a helicity control of the bare g-factor (Fig. 4c). In particular, linear fitting of the B dependence at 7.6 μW, away from the dip behaviour near 0 T, gives a larger g-factor for the σ^+ excitation under a negative B ($g_{-+} = -15.5$) and for the σ^- excitation under a positive B ($g_{+-} = -16.3$). On the contrary, the g factors of σ^- excitation under a negative B ($g_{--} = -9.2$) and σ^+ excitation under a positive B ($g_{++} = -9.6$) are smaller. We note that even with the observed non-linear behaviour at a higher circular power, the notion of a g-factor or linear-in-B splitting remains valid up to at least ±7 T. This behaviour can be empirically captured by assuming that the magnitude of B_{ex} increases linearly with $|B|$ (Supplementary Section 7).

In conclusion, we have demonstrated an optical generation of an exchange field in HBLs of semiconducting TMDs under a steady-state condition. This effective magnetic field, which arises from many-exciton interactions, can be dynamically tuned up to several tesla with very low continuous-wave incident powers (microwatts). Our experiments also motivate the exploration of strongly interacting quantum phases of light and matter under driven-dissipative conditions[31]. In particular, recent reports of exciton condensation and optical spectroscopy of strongly correlated electronic phases in moiré heterostructures of TMDs[38–41] make a strong case for investigating quantum magnetism with spin–valley pseudospins.

Online content

Any methods, additional references, Nature Research reporting summaries, source data, extended data, supplementary information, acknowledgements, peer review information; details of author contributions and competing interests; and statements of data and code availability are available at https://doi.org/10.1038/s41565-020-00804-0.

Received: 4 June 2020; Accepted: 26 October 2020;
Published online: 30 November 2020

References

1. Wang, G. et al. Colloquium: excitons in atomically thin transition metal dichalcogenides. *Rev. Mod. Phys.* **90**, 021001 (2018).
2. Xiao, D., Liu, G.-B., Feng, W., Xu, X. & Yao, W. Coupled spin and valley physics in monolayers of MoS_2 and other group-VI dichalcogenides. *Phys. Rev. Lett.* **108**, 196802 (2012).
3. Xiao, D., Yao, W. & Niu, Q. Valley-contrasting physics in graphene: magnetic moment and topological transport. *Phys. Rev. Lett.* **99**, 236809 (2007).
4. Kim, J. et al. Ultrafast generation of pseudo-magnetic field for valley excitons in WSe_2 monolayers. *Science* **346**, 1205–1208 (2014).
5. Sie, E. J. et al. Valley-selective optical stark effect in monolayer WS_2. *Nat. Mater.* **14**, 290–294 (2015).
6. Srivastava, A. et al. Valley Zeeman effect in elementary optical excitations of monolayer WSe_2. *Nat. Phys.* **11**, 141–147 (2015).
7. Aivazian, G. et al. Magnetic control of valley pseudospin in monolayer WSe_2. *Nat. Phys.* **11**, 148–152 (2015).
8. Li, Y. et al. Valley splitting and polarization by the Zeeman effect in monolayer $MoSe_2$. *Phys. Rev. Lett.* **113**, 266804 (2014).
9. MacNeill, D. et al. Breaking of valley degeneracy by magnetic field in monolayer $MoSe_2$. *Phys. Rev. Lett.* **114**, 037401 (2015).
10. Nagler, P. et al. Giant magnetic splitting inducing near-unity valley polarization in van der Waals heterostructures. *Nat. Commun.* **8**, 1551 (2017).
11. Wang, T. et al. Giant valley-Zeeman splitting from spin-singlet and spin-triplet interlayer excitons in $WSe_2/MoSe_2$ heterostructure. *Nano Lett.* **20**, 694–700 (2020).
12. Ciarrocchi, A. et al. Polarization switching and electrical control of interlayer excitons in two-dimensional van der Waals heterostructures. *Nat. Photon.* **13**, 131–136 (2019).
13. Zhang, J. et al. Enhancing and controlling valley magnetic response in MoS_2/WS_2 heterostructures by all-optical route. *Nat. Commun.* **10**, 4226 (2019).
14. Sanchez, O. L., Ovchinnikov, D., Misra, S., Allain, A. & Kis, A. Valley polarization by spin injection in a light-emitting van der Waals heterojunction. *Nano Lett.* **16**, 5792–5797 (2016).
15. Zhao, C. et al. Enhanced valley splitting in monolayer WSe_2 due to magnetic exchange field. *Nat. Nanotechnol.* **12**, 757 (2017).
16. Seyler, K. L. et al. Valley manipulation by optically tuning the magnetic proximity effect in WSe_2/CrI_3 heterostructures. *Nano Lett.* **18**, 3823–3828 (2018).
17. Li, W., Lu, X., Dubey, S., Devenica, L. & Srivastava, A. Dipolar interactions between localized interlayer excitons in van der Waals heterostructures. *Nat. Mater.* **19**, 624–629 (2020).
18. Kremser, M. et al. Discrete interactions between a few interlayer excitons trapped at a $MoSe_2$–WSe_2 heterointerface. *npj 2D Mater. Appl.* **4**, 8 (2020).
19. Rivera, P. et al. Valley-polarized exciton dynamics in a 2D semiconductor heterostructure. *Science* **351**, 688–691 (2016).
20. Laikhtman, B. & Rapaport, R. Exciton correlations in coupled quantum wells and their luminescence blue shift. *Phys. Rev. B* **80**, 195313 (2009).
21. Viña, L. et al. Spin splitting in a polarized quasi-two-dimensional exciton gas. *Phys. Rev. B* **54**, R8317 (1996).
22. Amand, T. et al. Spin relaxation in polarized interacting exciton gas in quantum wells. *Phys. Rev. B* **55**, 9880 (1997).
23. Ciuti, C., Savona, V., Piermarocchi, C., Quattropani, A. & Schwendimann, P. Role of the exchange of carriers in elastic exciton–exciton scattering in quantum wells. *Phys. Rev. B* **58**, 7926 (1998).
24. Hong, X. et al. Ultrafast charge transfer in atomically thin MoS_2/WS_2 heterostructures. *Nat. Nanotechnol.* **9**, 682 (2014).
25. Zhu, H. et al. Interfacial charge transfer circumventing momentum mismatch at two-dimensional van der Waals heterojunctions. *Nano Lett.* **17**, 3591–3598 (2017).
26. Tran, K. et al. Evidence for moiré excitons in van der Waals heterostructures. *Nature* **567**, 71–75 (2019).
27. Jiang, C. et al. Optical spin pumping induced pseudomagnetic field in two-dimensional heterostructures. *Phys. Rev. B* **98**, 241410 (2018).
28. Tan, L. B. et al. Interacting polaron–polaritons. *Phys. Rev. X* **10**, 021011 (2020).
29. Back, P., Zeytinoglu, S., Ijaz, A., Kroner, M. & Imamoğlu, A. Realization of an electrically tunable narrow-bandwidth atomically thin mirror using monolayer $MoSe_2$. *Phys. Rev. Lett.* **120**, 037401 (2018).
30. Scuri, G. et al. Large excitonic reflectivity of monolayer $MoSe_2$ encapsulated in hexagonal boron nitride. *Phys. Rev. Lett.* **120**, 037402 (2018).
31. Barachati, F. et al. Interacting polariton fluids in a monolayer of tungsten disulfide. *Nat. Nanotechnol.* **13**, 906–909 (2018).
32. Wang, G. et al. Magneto-optics in transition metal diselenide monolayers. *2D Mater.* **2**, 034002 (2015).
33. Stier, A. V., McCreary, K. M., Jonker, B. T., Kono, J. & Crooker, S. A. Exciton diamagnetic shifts and valley Zeeman effects in monolayer WS_2 and MoS_2 to 65 Tesla. *Nat. Commun.* **7**, 10643 (2016).
34. Lyons, T. P. et al. The valley Zeeman effect in inter- and intra-valley trions in monolayer WSe_2. *Nat. Commun.* **10**, 2330 (2019).
35. Wang, Z., Mak, K. F. & Shan, J. Strongly interaction-enhanced valley magnetic response in monolayer WSe_2. *Phys. Rev. Lett.* **120**, 066402 (2018).
36. Smoleński, T. et al. Tuning valley polarization in a WSe_2 monolayer with a tiny magnetic field. *Phys. Rev. X* **6**, 021024 (2016).
37. Jiang, C. et al. Microsecond dark-exciton valley polarization memory in two-dimensional heterostructures. *Nat. Commun.* **9**, 753 (2018).
38. Wang, Z. et al. Evidence of high-temperature exciton condensation in two-dimensional atomic double layers. *Nature* **574**, 76–80 (2019).
39. Tang, Y. et al. Simulation of Hubbard model physics in WSe_2/WS_2 moiré superlattices. *Nature* **579**, 353–358 (2020).
40. Regan, E. C. et al. Mott and generalized Wigner crystal states in WSe_2/WS_2 moiré superlattices. *Nature* **579**, 359–363 (2020).
41. Shimazaki, Y. et al. Strongly correlated electrons and hybrid excitons in a moiré heterostructure. *Nature* **580**, 472–477 (2020).

Methods

Sample fabrication. We transferred the mechanically exfoliated samples by a polydimethylsiloxane-based dry-transfer method on 300 nm SiO_2/Si substrates. Monolayer $MoSe_2$ (HQ graphene) was stacked on top of monolayer WSe_2 (HQ graphene) with the edges aligned. After the stacking, the sample was annealed in 5% H_2/95% N_2 at 125 °C for 2 h.

Magneto-optical spectroscopy. We used two homebuilt, low-temperature (~4 K) confocal microscope set-ups for the magneto-photoluminescence measurements. The sample was first loaded into a closed-cycle cryostat (AttoDry 800, base temperature ~4 K) for the sample characterization and subsequently into another cryostat (BlueFors cryogenics, base temperature ~3.2 K) for Faraday geometry measurements (from −8 to +8 T). The sample was positioned by a coarse and fine piezoelectric nanopositioners (Attocube systems). The emission was collected using either a room- or low-temperature achromatic objective (NA = 0.42 for AttoDry 800 and 0.63 for BlueFors cryogenics) and directed to a high-resolution (focal lengths of 500 mm for AttoDry 800 and 750 mm for BlueFors cryogenics) spectrometer (Princeton Instrument HR-500 for AttoDry 800 and Princeton Instruments SP-2750i for BlueFors cryogenics), in which it was dispersed by a 1,200 or 300 g mm^{-1} grating (both blazed at 750 nm). A charge coupled device (Princeton Instrument PIXIS-400 CCD for AttoDry 800 and PyLoN CCD for BlueFors cryogenics) was used as the detector. The excitation laser was a mode-hop-free tunable continuous-wave Ti:sapphire laser (MSquared Lasers) with a resolution of 0.1 pm, which was focused to a spot size of 1 μm on the sample. The polarization of the incident laser was controlled by using a polarizer together with a liquid crystal variable retarder ($\lambda/4$ waveplate) for Bluefors cryogenics (AttoDry 800). Polarization-resolved measurements were performed by using a $\lambda/4$ waveplate (achromatic, 690–1,200 nm) placed before a Wollaston prism. The mechanism was that $\lambda/4$ waveplate-transformed circular emission was converted into the *s* and *p* components of linearly polarized light, and then the two components were displaced separately by a Wollaston prism. Another achromatic $\lambda/4$ waveplate was placed after the Wollaston prism to convert the linearly polarized light into a circular signal, to avoid the polarization sensitivity of the grating.

Data availability

The authors declare that the data supporting the findings of this study are available within the paper, Supplementary Information and Source Data. Extra data are available from the corresponding authors upon request. Source data are provided with this paper.

Acknowledgements

We acknowledge many enlightening discussions with A. Imamoğlu. A.S. acknowledges support from the NSF through the EFRI program, grant no. EFMA-1741691, and from NSF DMR award no. 1905809.

Author contributions

W.L., X.L. and J.W. contributed equally to this work. A.S., W.L. and X.L. conceived the project. W.L., X.L. and J.W. carried out the measurements. J.W. prepared the samples. A.S. supervised the project. All the authors were involved in the analysis of the experimental data and contributed extensively to this work.

Competing interests

The authors declare no competing interests.

Additional information

Supplementary information is available for this paper at https://doi.org/10.1038/s41565-020-00804-0.

Correspondence and requests for materials should be addressed to A.S.

Nature Nanotechnology thanks the anonymous reviewers for their contribution to the peer review of this work.

Reprints and permissions information is available at www.nature.com/reprints.